

# Multipolar Fermi-surface deformation in a Rydberg-dressed Fermi gas with long-range anisotropic interactions

Yijia Zhou<sup>1,2</sup>, Rejish Nath<sup>3</sup>, Haibin Wu<sup>4,5</sup>, Igor Lesanovsky<sup>1,6</sup>, Weibin Li<sup>1</sup>

<sup>1</sup>*School of Physics and Astronomy and Centre for the Mathematics and Theoretical Physics of Quantum Non-equilibrium Systems, University of Nottingham, Nottingham NG7 2RD, United Kingdom*

<sup>2</sup>*Graduate School of China Academy of Engineering Physics, Beijing 100193, China*

<sup>3</sup>*Department of Physics, Indian Institute of Science Education and Research, Dr. Homi Bhabha Road, Pune 411008, Maharashtra, India*

<sup>4</sup>*State Key Laboratory of Precision Spectroscopy, East China Normal University, Shanghai 200062, China*

<sup>5</sup>*Collaborative Innovation Center of Extreme Optics, Shanxi University, Taiyuan 030006, China*

<sup>6</sup>*Institut für Theoretische Physik, University of Tübingen, 72076 Tübingen, Germany*

(Dated: December 28, 2021)

We study theoretically the deformation of the Fermi surface (FS) of a three-dimensional gas of Rydberg-dressed <sup>6</sup>Li atoms. The laser dressing to high-lying Rydberg  $D$  states results in angle-dependent soft-core-shaped interactions whose anisotropy is described by multiple spherical harmonics. We show that this can drastically modify the shape of the FS and that its deformation depends on the interplay between the Fermi momentum  $k_F$  and the reciprocal momentum  $\bar{k}$  corresponding to the characteristic soft-core radius of the dressing-induced potential. When  $k_F < \bar{k}$ , the dressed interaction stretches a spherical FS into an ellipsoid. When  $k_F \gtrsim \bar{k}$ , complex deformations are encountered which exhibit multipolar characteristics. We analyze the formation of Cooper pairs around the deformed FS and show that they occupy large orbital angular momentum states ( $p$ ,  $f$ , and  $h$  wave) coherently. Our study demonstrates that Rydberg dressing to high angular momentum states may pave a route toward the investigation of unconventional Fermi gases and multiwave superconductivity.

*Introduction.* Fermi surfaces (FSs), describing the occupation of momentum space by fermions, lie at the heart of Fermi liquid theory [1]. Though typically being a sphere in free space, FSs can be deformed by anisotropic two-body interactions, resulting in novel physics, manifesting in the nematic phase [2] and the Pomeranchuk instability [3]. Quantum simulators based on ultracold atoms provide a flexible platform for realizing Fermi gases with controllable FS [4]. Spherical FSs have been observed in free [5] and weakly interacting gases [6]. The spherical symmetry can be broken by anisotropic dipole-dipole interactions [7–13], and the deformation of the FS from a sphere to ellipsoid [14–22] has been observed in polarized dipolar gases [23].

A newly emerged approach to creating long-range interactions is so-called Rydberg dressing [24–29]: Using off-resonant lasers, the strong van der Waals interaction between electronically high-lying Rydberg atoms [30–32] is mapped to the ground state, yielding an effective interaction between dressed atoms that possesses a characteristic “soft-core” shape. The radius  $\bar{R}$  at which the soft core occurs [25] and the potential shape can be tuned by dressing to different Rydberg states [33–37]. Generically, the collective behavior of the atomic gas is strongly impacted by the soft-core interaction [25, 27, 35, 38]. In particular, the stability of elementary excitation and the emergence of supersolidity is connected to  $\bar{R}$ . So far experimental and theoretical studies have mostly focused on spin [39–41] and bosonic systems [25–29, 42–44]. In a recent experiment [45], dressing of the fermionic <sup>6</sup>Li atoms to Rydberg  $P$  states was demonstrated, which indeed highlighted new opportunities for the exploration of correlated many-body phases with Rydberg-dressed fermions [46–50].

In this work, we study the FS deformation of a spin-polarized, zero-temperature gas of <sup>6</sup>Li atoms through Rydberg dressing. We find that the emerging long-range attrac-

tive two-body interaction  $V(\mathbf{r})$  combines monopole, dipole, and quadrupole components [Fig. 1(a)], when dressing the ground-state atoms to a high-lying Rydberg  $D$  state. In momentum space, the interaction  $V(\mathbf{k})$  is largest at around  $k(\theta) = 5\pi/3R(\theta)$  with  $R(\theta)$  being the angle-dependent soft-core radius [Fig. 1(b)]. When the Fermi momentum becomes larger than the minimum  $k(\theta)$ , the FS is strongly deformed and gains multipolar symmetries. We show that this deformation is accompanied by the formation of Cooper pairs, where  $p$ -,  $f$ -, and  $h$ -wave pairing coexist coherently when multipolar FS deformation occurs. The  $p$ - and  $f$ -wave pairing are key to the superfluidity of <sup>3</sup>He [51, 52] and unconventional superconductors as shown in Ref. [53], while  $h$ -wave pairing has, to the best of our knowledge, not been identified in any other system. Our work shows that Rydberg-dressed fermions provide a tunable quantum simulator for investigating novel FS deformation and nontrivial pairing states.

*Anisotropic Rydberg-dressed interaction.* In our setting, each Li<sup>6</sup> atom consists of the electronic ground state  $|g\rangle = |2S_{1/2}\rangle$ , intermediate state  $|e\rangle = |2P_{3/2}\rangle$ , and Rydberg state  $|r\rangle = |nD_{5/2}\rangle$  ( $n$  denotes the principal quantum number), as shown in Fig. 2(a). A probe and a control laser couple the  $|g\rangle \leftrightarrow |e\rangle$  and  $|e\rangle \leftrightarrow |r\rangle$  transitions. This coupling is described by the single-atom Hamiltonian  $\hat{H}^{(1)} = \delta_p|e\rangle\langle e| + (\delta_p + \delta_c)|r\rangle\langle r| + (\Omega_p/2)(|g\rangle\langle e| + |e\rangle\langle g|) + (\Omega_c/2)(|e\rangle\langle r| + |r\rangle\langle e|)$ , where  $\Omega_p$  ( $\Omega_c$ ) and  $\delta_p$  ( $\delta_c$ ) are Rabi frequency and detuning of the probe (control) laser, respectively. The state  $|e\rangle$  can be adiabatically eliminated, provided that  $|\delta_p| \gg |\Omega_p|$ ,  $|\Omega_c|$ , and  $|\delta_c|$ . This leads to an effective Hamiltonian,  $\hat{H}_e^{(1)} \approx \delta|r\rangle\langle r| - \Omega/2(|g\rangle\langle r| + |r\rangle\langle g|)$  with the effective detuning  $\delta \approx \delta_p + \delta_c - (\Omega_c^2 - \Omega_p^2)/(4\delta_p)$ , and Rabi frequency  $\Omega = \Omega_p\Omega_c/(2\delta_p)$ .

When excited to the Rydberg state, two atoms interact through the angular dependent van der Waals (vdW) inter-

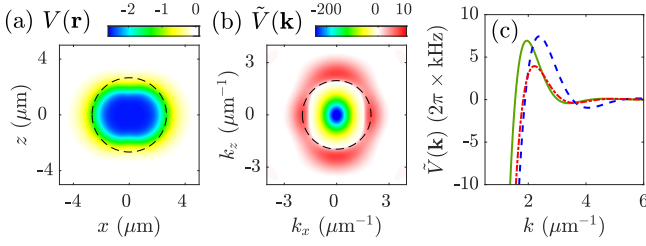


FIG. 1. Anisotropic soft-core interaction through Rydberg-dressing. (a) Angular dependence of the attractive, soft-core interaction  $V(d, \theta)$  in the  $xz$  plane. The interaction is stronger (weaker) along the  $x(z)$  axis. The dashed line shows the circle whose radius is  $\bar{R}$ . (b) The Fourier transformed potential  $\tilde{V}(\mathbf{k})$  is attractive at small momentum and becomes repulsive around  $\bar{k} \approx 5\pi/(3\bar{R})$  (dashed line). (c) Profile of  $\tilde{V}(\mathbf{k})$  cuts along the polar angle  $\theta_k = 0$  (blue dashed),  $\pi/2$  (green solid), and  $\pi$  (red dash-dot). We consider  $n = 40$ ,  $V_0 \approx -2\pi \times 2.53$  kHz, and  $\delta = -2\pi \times 40$  MHz. The energy unit in panels (a) and (b) is  $2\pi \times$  kHz. See text for details.

action  $V_{\text{vdW}}(d, \theta) = C_6(\theta)/d^6$ , where  $C_6(\theta)$  is the dispersion coefficient,  $d = |\mathbf{r} - \mathbf{r}'|$  is the distance between the atoms (locating at  $\mathbf{r}$  and  $\mathbf{r}'$ ), and  $\theta$  is the angle between the atoms and quantization  $z$  axis [see Fig. 2(b)]. We obtain the two-atom Hamiltonian,  $\hat{H}^{(2)} = \hat{H}_e^{(1)}(\mathbf{r}) + \hat{H}_e^{(1)}(\mathbf{r}') + V_{\text{vdW}}(d, \theta)|rr\rangle\langle rr|$ . In  $|nD_{5/2}, 5/2\rangle$  states of  ${}^6\text{Li}$  atoms, the dispersion coefficient can be expressed in terms of spherical harmonics  $Y_{lm}(\theta)$  ( $l$  is an even number)

$$C_6(\theta) = C_0 Y_{00}(\theta) + C_2 Y_{20}(\theta) + C_4 Y_{40}(\theta), \quad (1)$$

which consists of monopole, dipole and quadrupole components [54] with strength  $[C_0, C_2, C_4] = [-17.32, 5.98, -0.076] \times 10^{-17} n^{11} \text{GHz } \mu\text{m}^6$  [55].

When  $|\delta| \gg |\Omega|$ , the ground-state atoms are weakly coupled to the Rydberg state, such that they experience a weaker, laser-dressed two-body interaction. The dressed interaction can be obtained through the conventional fourth-order perturbation calculation [25, 56]. One can also derive the dressed interaction through the projection operator method [57]. We first define the two-atom ground-state subspace given by  $\hat{P} =$

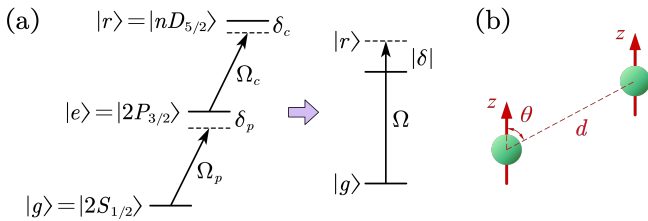


FIG. 2. Rydberg dressing. (a) Two-photon dressing scheme. The probe laser is far and blue detuned while the control laser is on resonance. The three-level system can be simplified to a two-level model by adiabatic elimination. The effective Rabi frequency is  $\Omega = \Omega_p \Omega_c / (2\delta_p)$ , and the effective detuning is  $\delta = \delta_p + \delta_c - (\Omega_c^2 - \Omega_p^2) / (4\delta_p)$ . (b) Displacement between two atoms, and  $\theta$  is the angle between the displacement and quantization axis.

$|gg\rangle\langle gg|$ . The effective Hamiltonian in this subspace is

$$\hat{H}_{\text{eff}} = \hat{P} \hat{H} \hat{P} - \hat{P} \hat{H} \hat{Q} \frac{1}{\hat{Q} \hat{H} \hat{Q}} \hat{Q} \hat{H} \hat{P}, \quad (2)$$

where  $\hat{Q} = \hat{\mathbb{I}} - \hat{P}$  with  $\hat{\mathbb{I}}$  being the identity operator. This results to the dressed interaction potential

$$V(d, \theta) = V_0 \frac{R^6(\theta)}{d^6 + R^6(\theta)}, \quad (3)$$

in which the soft-core radius  $R(\theta) = \sqrt[6]{C_6(\theta)/(2\delta)}$  depends on the state- and angle-dependent dispersion coefficient  $C_6(\theta)$ , and the strength  $V_0 = \Omega^4/(8\delta^3)$ . The detuning  $\delta$  and the potential depth  $V_0$  can be controlled by the dressing laser [55]. When  $C_6(\theta) < 0$  and  $\delta < 0$ , the dressed interaction is attractive everywhere. Moreover, it is of cylindrical symmetry with respect to the  $z$  axis [Fig. 1(a)], as  $C_6(\theta)$  has no dependence on the azimuth angle [as  $m = 0$  for all  $Y_{lm}(\theta)$  of Eq. (1)].

Although  $V(d, \theta)$  is attractive for all interparticle distance  $d$ , its Fourier transform,  $\tilde{V}(\mathbf{k})$ , is attractive when  $k(\theta_k)$  is small and becomes positive when  $k(\theta_k) > 1.37\pi/R(\theta_k)$  [Fig. 1(b)]. It reaches the maximum around  $k(\theta_k) \approx 5\pi/3R(\theta_k)$  [Fig. 1(c)]. As we will show later, the positive region turns out to be important in determining the ground state of the Fermi gas. For convenience, we will use  $\bar{k} \approx 5\pi/3\bar{R}$  as the characteristic momentum, where  $\bar{R} = R(\pi/2)$  is the soft-core radius along the  $x$  axis [Fig. 1(a)].  $\tilde{V}(k)$  depends on the modulus  $|k|$  as well as on the polar angle (in  $k$  space)  $\theta_k$ . This is in contrast to dipolar interactions whose Fourier transform is solely a function of the polar angle [7, 19].

*Modelling the Rydberg-dressed  ${}^6\text{Li}$  gas.* Our system is a three-dimensional (3D) homogeneous gas of  $N$  dressed  ${}^6\text{Li}$  atoms, whose Hamiltonian is given by

$$H = \int d\mathbf{r} \hat{\psi}^\dagger(\mathbf{r}) \left[ -\frac{\hbar^2}{2m} \nabla^2 - \mu \right] \hat{\psi}(\mathbf{r}) + \iint d\mathbf{r} d\mathbf{r}' \hat{\psi}^\dagger(\mathbf{r}) \hat{\psi}^\dagger(\mathbf{r}') V(d, \theta) \hat{\psi}(\mathbf{r}') \hat{\psi}(\mathbf{r}), \quad (4)$$

where the operator  $\hat{\psi}(\mathbf{r})$  annihilates a Fermion with mass  $m$  at position  $\mathbf{r}$ . The first line of the above Hamiltonian gives the usual kinetic energy and chemical potential  $\mu$ . The second line describes the interaction between two Fermions at positions  $\mathbf{r}$  and  $\mathbf{r}'$  via the soft-core potential. Using the plane-wave basis, the Hamiltonian can be re-expressed as,

$$H = \int \frac{d^3\mathbf{k}}{(2\pi)^3} \left( \frac{\hbar^2 |\mathbf{k}|^2}{2m} - \mu \right) \hat{a}_{\mathbf{k}}^\dagger \hat{a}_{\mathbf{k}} + \iiint \frac{d^3\mathbf{k}}{(2\pi)^3} \frac{d^3\mathbf{k}'}{(2\pi)^3} \frac{d^3\mathbf{q}}{(2\pi)^3} \hat{a}_{\mathbf{k}+\mathbf{q}}^\dagger \hat{a}_{\mathbf{k}'}^\dagger \tilde{V}(\mathbf{q}) \hat{a}_{\mathbf{k}'+\mathbf{q}} \hat{a}_{\mathbf{k}}, \quad (5)$$

where  $\hat{a}_{\mathbf{k}} = \int d^3\mathbf{r} \hat{\psi}(\mathbf{r}) e^{-i\mathbf{k}\cdot\mathbf{r}}$  ( $\hat{a}_{\mathbf{k}}^\dagger = \int d^3\mathbf{r} \hat{\psi}^\dagger(\mathbf{r}) e^{i\mathbf{k}\cdot\mathbf{r}}$ ) is the annihilation (creation) operator of a Fermion with momentum  $\mathbf{k}$ .

To understand the impact of the anisotropic interaction on the many-body physics, we study the ground state of

the system within the Hartree-Fock-Bogoliubov (HFB) approach [21, 58]. Assuming pairing occurs between particles with momentum  $\mathbf{k}$  and  $-\mathbf{k}$ , this allows to write down the BCS wave function  $|G\rangle_{\text{BCS}} = \prod_{\mathbf{k}} (u_{\mathbf{k}} + v_{\mathbf{k}} \hat{a}_{\mathbf{k}}^\dagger \hat{a}_{-\mathbf{k}}^\dagger) |0\rangle$ . The ground state is determined by the approximate HFB Hamiltonian,

$$H_{\text{HFB}} = \int \frac{d^3\mathbf{k}}{(2\pi)^3} \xi_{\mathbf{k}} \hat{a}_{\mathbf{k}}^\dagger \hat{a}_{\mathbf{k}} + [\Delta(\mathbf{k}) \hat{a}_{\mathbf{k}}^\dagger \hat{a}_{-\mathbf{k}}^\dagger + \text{H.c.}], \quad (6)$$

where  $\xi_{\mathbf{k}} = \varepsilon_{\mathbf{k}} + U_e(\mathbf{k}) + U_d - \mu$  with  $\varepsilon_{\mathbf{k}} = \hbar^2|\mathbf{k}|^2/2m$  being the kinetic energy of free fermions. The Hartree energy  $U_d = N\tilde{V}(0)$  is a constant and can be absorbed into the chemical potential. Both the Fock energy  $U_e(\mathbf{k}) = -\sum_{\mathbf{k}'} \tilde{V}(\mathbf{k}-\mathbf{k}') \langle \hat{a}_{\mathbf{k}'}^\dagger \hat{a}_{\mathbf{k}'} \rangle$  and the gap function  $\Delta(\mathbf{k}) = \sum_{\mathbf{k}'} \tilde{V}(\mathbf{k}-\mathbf{k}') \langle \hat{a}_{-\mathbf{k}'}^\dagger \hat{a}_{\mathbf{k}'} \rangle$  depend on  $\tilde{V}(\mathbf{k})$ . The shape of the interaction, i.e.,  $\tilde{V}(-\mathbf{k}) = \tilde{V}(\mathbf{k})$ , implies  $U_e(-\mathbf{k}) = U_e(\mathbf{k})$  and  $\Delta(-\mathbf{k}) = -\Delta(\mathbf{k})$ . In the absence of two-body interaction,  $\tilde{V}(\mathbf{k}) = 0$ , one obtains a spherical FS of radius  $k_F = (6\pi^2\rho)^{1/3}$  ( $\rho$  is the real space density) in momentum space, where the density distribution is  $\tilde{\rho}_0(\mathbf{k}) = \Theta(k_F - |\mathbf{k}|)$  in the ground-state with  $\Theta(\cdot)$  to be the Heaviside function. As the variational parameter  $u_{\mathbf{k}}$  and  $v_{\mathbf{k}}$  satisfy

$$u_{\mathbf{k}}^2 = \frac{1}{2} \left[ 1 + \frac{\xi_{\mathbf{k}}}{\sqrt{\xi_{\mathbf{k}}^2 + |\Delta_{\mathbf{k}}|^2}} \right], \quad v_{\mathbf{k}}^2 = \frac{1}{2} \left[ 1 - \frac{\xi_{\mathbf{k}}}{\sqrt{\xi_{\mathbf{k}}^2 + |\Delta_{\mathbf{k}}|^2}} \right],$$

we can obtain the BCS ground state by solving the gap function self-consistently.

*Multipolar FS deformation.* We first illustrate with examples that the anisotropic Rydberg-dressed interaction can break the spherical symmetry of the FSs for noninteracting fermions. In Fig. 3(a1), we show the momentum distribution for  $n = 25$  (i.e., the atoms are dressed to the  $|25D_{5/2}, 5/2\rangle$  state), which displays a sharp edge at the FS. The FS is slightly deformed from a sphere, which is confirmed by a numerical fit of the FS based on the conventional mean-field solution (see the Supplemental Material, SM, for details [55]). This anisotropy results from the fact that the scattering of two atoms does not preserve each of their orbital angular momenta due to the anisotropic dressed interaction [59]. However the difference of the momentum distribution from the interaction-free one, given by  $\delta\tilde{\rho}(\mathbf{k}) = \tilde{\rho}(\mathbf{k}) - \tilde{\rho}_0(\mathbf{k})$ , is marginal for the low-lying  $n = 25$  state [Fig. 3(a2)].

The momentum distribution changes qualitatively with increasing principal quantum number  $n$ . For  $n = 35$  [Fig. 3(b1)] and 55 [Fig. 3(c1)], the Fermi sea is depleted notably around  $k_F$ . Importantly, the momentum distributions become strongly anisotropic. To quantify the anisotropy of  $\tilde{\rho}(\mathbf{k})$ , we first evaluate its angular distribution by integrating over the radial part,  $\chi(\theta_k) = 2\pi/N \int \tilde{\rho}(\mathbf{k}) k^2 dk$  with the normalization condition  $\int_0^\pi \chi(\theta_k) \sin\theta_k d\theta_k = 1$ . Here, the azimuthal angle  $\phi_k$  has been integrated out straightly due to the cylindrical symmetry of  $\tilde{\rho}(\mathbf{k})$ . Then the angular function is expanded in terms of spherical harmonics,  $\chi(\theta_k) = \sum_{l=0,2,4,\dots} \lambda_l Y_{l0}(\theta_k)$  where  $\lambda_l = \int \chi(\theta_k) Y_{l0}(\theta_k) \sin\theta_k d\theta_k$  [55] is the coefficient of  $\chi(\theta_k)$  projected to  $Y_{l0}(\theta_k)$ . Here, a nonvanishing  $\lambda_l$  ( $l > 0$ ) means that

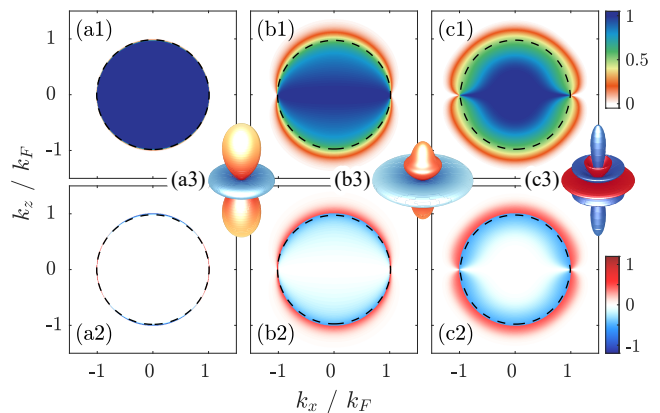


FIG. 3. State-dependent FS deformation. Density distribution in momentum space for (a1)  $n = 25$  with  $\bar{R} = 1.12 \mu\text{m}$ , (b1)  $n = 35$  with  $\bar{R} = 2.08 \mu\text{m}$ , and (c1)  $n = 55$  with  $\bar{R} = 4.77 \mu\text{m}$ . The corresponding  $\delta\tilde{\rho}(\mathbf{k})$  is given in panels (a2), (b2), and (c2). The dashed line in the first and second row is the fitted FS (see SM [55] for details), which locates the momentum where  $\delta\tilde{\rho}(\mathbf{k}) \approx 0$ . For  $n = 25$ , the deformation of the FS is described by the spherical harmonics  $Y_{20}(\theta_k)$ , shown in panel (a3). For  $n = 35$  and 55, the FS deformation has complicated multipolar features, as shown in panels (b3) and (c3), respectively. Here  $k_F = 2 \mu\text{m}^{-1}$ , and other parameters are same with Fig. 1.

the shape of the FS is not spherical. For parameters considered in this work, it is found that  $\lambda_l$  becomes negligible when  $l > 6$ .

The main result of this work is that the shape of the FS involves multiple  $\lambda_l$ . As shown in Fig. 4(a),  $\lambda_2$  is the only nonzero projection coefficient when  $k_F \bar{R} < 3$  ( $k_F \lesssim 0.6\bar{k}$ ) and assumes its maximal value around  $k_F \bar{R} \approx 3$ . In this region, we obtain a *dipolar deformation* ( $l = 2$ ), where the FS is stretched in the  $k_z$  direction [Fig. 3(a3)], and becomes an ellipsoid. When  $k_F \bar{R} > 3$ , the amplitudes of  $\lambda_4$  and  $\lambda_6$  increase while the one for  $\lambda_2$  decreases. In the region  $3.5 \lesssim k_F \bar{R} \lesssim 5$ ,  $|\lambda_4|$  and  $\lambda_6$  become comparable to  $\lambda_2$ . In this *multipolar deformation* regime, mainly three spherical harmonics contribute to the FS:  $Y_{20}(\theta_k)$ ,  $Y_{40}(\theta_k)$ , and  $Y_{60}(\theta_k)$  [Fig. 3(b3)]. When further increasing  $k_F \bar{R} > 6$ , the value of all  $\lambda_l$  decreases and saturates. As  $|\lambda_4| > |\lambda_6| > |\lambda_2|$ , this yields a FS deformation significantly different [Fig. 3(c3)] from the one shown in Fig. 3(a3).

The depletion of the momentum density becomes significant when the multipolar deformation is present. This leads to an increase of the variance  $\text{Var}(\tilde{\rho}) = \sum_{\mathbf{k}} [\tilde{\rho}(\mathbf{k}) - \tilde{\rho}_0(\mathbf{k})]^2 / \rho$  of the momentum distribution, as shown in the inset of Fig. 4(b). However, when  $n < 30$ , the variance is small and increases only slowly with  $n$ . When  $n > 30$ , it increases rapidly and saturates gradually, where the deformation is given mainly by the  $\lambda_6$  term [Fig. 4(a)].

*Scaling in the dipolar deformation regime.* The value of  $\lambda_2$ , which parametrizes the FS deformation, follows a power-law scaling with respect to the system parameters, such as the interaction strength  $V_0$ , the density of atoms  $\rho$ , and the interaction length  $\bar{R}$ . When  $\lambda_2$  dominates, we find that the density distribution changes rapidly at the FS which gives

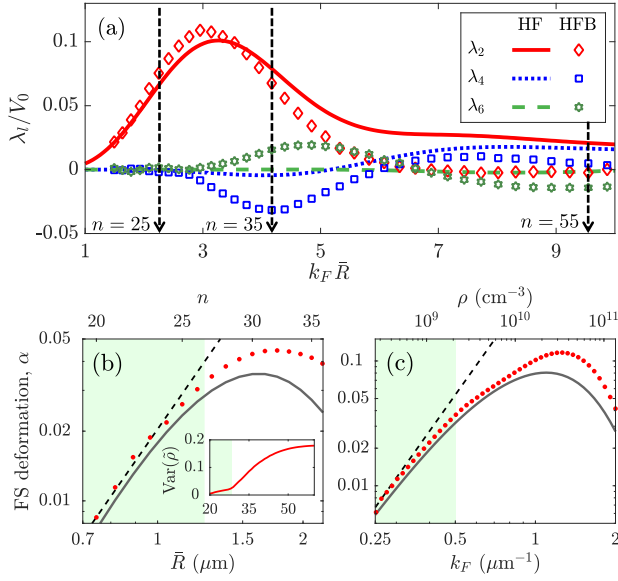


FIG. 4. Characterization of the multipolar FS. (a) The projection coefficient  $\lambda_j$  (diamond, square, star) and  $\lambda'_j$  (solid, dotted, dashed) based on the HFB and HF calculation. In the calculation, we vary  $\bar{R}$  (through  $n$ ) and fix  $k_F = 2 \mu\text{m}^{-1}$ .  $\lambda_2$  dominates when  $k_F \bar{R} < 3$  ( $n < 30$ ).  $\lambda_4$  and  $\lambda_6$  become important when  $k_F \bar{R} > 3$ , where the multipolar FS deformation emerges. When  $k_F \bar{R} \lesssim 3$ , the deformation of the FS can also be characterized by its ellipticity,  $\alpha = 1 - \mathbf{k}_F(0)/\mathbf{k}_F(\pi/2)$ . In panels (b) and (c), we show the ellipticity by changing the soft-core radius  $\bar{R}$  ( $n$ ) and  $k_F$  ( $\rho$ ), respectively. When  $\lambda_2$  dominates, one finds  $\alpha \approx 3\sqrt{5}/\pi\lambda_2/4$ , establishing a relation of the ellipticity and  $\lambda_2$ . The numerical data (dots) and perturbation results (solid) follow the power-law scaling well in the shaded area. The inset in panel (b) shows the variance of the density distribution  $\tilde{\rho}(\mathbf{k})$ . In (b)  $k_F = 2 \mu\text{m}^{-1}$  and (c)  $n = 35$ . Other parameters are same as in Fig. 1.

rise to a modified Fermi momentum  $\mathbf{k}'_F$  [Fig. 3(a1)]. This deformation is quantified by the deviation of  $\mathbf{k}'_F$  from  $k_F$ ,  $\delta\mathbf{k}_F = \mathbf{k}'_F - k_F\hat{\mathbf{n}}$ , where  $\hat{\mathbf{n}}$  is the unit vector parallel to  $\mathbf{k}'_F$ . As pairing is not important here,  $\delta\mathbf{k}_F$  can be evaluated from the Hartree-Fock energy [60, 61]

$$\frac{\delta\mathbf{k}_F}{k_F} \approx \frac{1}{2E_F} \int d^3\mathbf{q} \tilde{V}(\mathbf{k}'_F - \mathbf{q}) \tilde{\rho}(\mathbf{q}). \quad (7)$$

Assuming  $\tilde{\rho}(\mathbf{q}) \approx \tilde{\rho}_0(\mathbf{q})$  and projecting  $\delta\mathbf{k}_F$  onto spherical harmonics, this yields

$$\frac{\delta\mathbf{k}_F}{k_F} \approx \frac{4\pi}{3} \sum_{l=2,4,6} \lambda_l Y_{l0}(\theta_k), \quad (8)$$

with  $\lambda_l = 3/(8\pi E_F) \int_0^\infty F_l(k/k_F \bar{R}) G_l(k) dk$  being the approximate projection coefficient. Here, we have defined  $F_l(k) = \int_0^\pi Y_{l0}(\theta_k) V(k\bar{R}, \theta_k) \sin\theta_k d\theta_k$  and  $G_l(k) = 4i^l k j_1(k) j_l(k)$ , where  $j_l(k)$  is the spherical Bessel function of the first kind (see the SM [55]).

As shown in Fig. 4(a), the coefficient  $\lambda_2$ , obtained from the perturbative calculation agrees well with the full-numerical method up to  $k_F \bar{R} \approx 3$ . In this region, we can make a Taylor expansion of  $\lambda_2$  in terms of  $k_F \bar{R}$ , whose leading term is

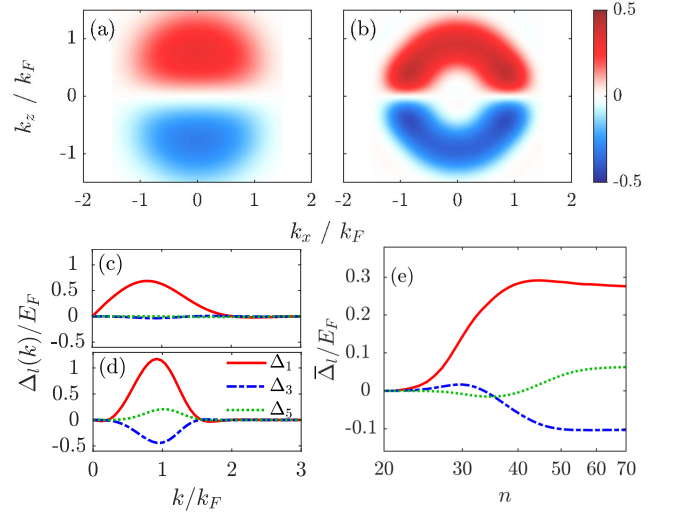


FIG. 5. Cooper pairs of multiple partial waves. Gap functions  $\Delta(\mathbf{k})$  for (a)  $n = 35$  and (b)  $n = 55$ . The projection of  $\Delta(\mathbf{k})$  to the spherical harmonics  $Y_{l0}$  ( $l$  odd) for (b)  $n = 35$  and (c)  $n = 55$ , respectively. For panel (c),  $n = 35$ , the gap function is occupied by the  $p$ -wave component. For panel (d),  $n = 55$ , it turns out that  $f$ -wave ( $l = 3$ ) and  $h$ -wave ( $l = 5$ ) pairing become important as well. (e) The population of various pair states as a function of quantum number  $n$ . Note that  $f$ - and  $h$ -wave pairing are non-negligible when  $n > 40$ . Other parameters are the same as those in Figs. 4(b) and 4(c), respectively.

$\lambda_2 \propto V_0(k_F \bar{R})^5/E_F$  [55]. This results in the power law relations  $\lambda_2 \propto \bar{R}^3, n^{11/2}, k_F^3$ . This scaling matches with the numerical calculations when  $k_F \bar{R}$  is small, as shown by the shaded area in Figs. 4(b) and 4(c). Experimentally, the predicted scaling can be measured by tuning the atomic density ( $k_F$ ) and laser parameters ( $n$  and  $\delta$ ) jointly or separately, which is useful in exploring the FS deformation and the dressed interaction experimentally. Finally, we note that the peak at  $k_F \bar{R} \approx 3$  can also be explained within the perturbative treatment pursued here:  $F_2[k/(k_F \bar{R})]$  has a single peak located at  $k = k_F \bar{R}$ , and  $G_2(k)$  oscillates with  $k$ , as discussed in the SM [55]. We thus obtain the maximal  $\lambda_2$  when the peaks of  $F_2(k)$  and  $G_2(k)$  coincide at  $k_F \bar{R} \approx 3$ .

*Cooper pairing in the multipolar deformation regime.* In the HFB approach, the gap function  $\Delta(\mathbf{k})$  serves as an order parameter of superfluidity. Here the superfluid is formed by Cooper pairs of two fermionic atoms with opposite momenta [21, 59]. In Fig. 5(a), we show the distribution of the gap function  $\Delta(\mathbf{k})$  for  $n = 35$ . It is nonzero in a wide region around the FS where the momentum density differs drastically from the interaction-free Fermi sea [Fig. 3(b1)]. Here an antisymmetry of the gap function is observed along the  $k_z$  axis. For  $n = 55$  [Fig. 5(b)], the pair distribution becomes more confined around the FS, and its peak value increases [Fig. 3(c1)].

To gain further insights of the pairing, we expand the gap function into partial waves,  $\Delta(\mathbf{k}) = \sum_l \Delta_l(k) Y_{lm}(\theta_k)$  with  $\Delta_l(k) = \int \Delta(\mathbf{k}) Y_{lm}(\theta_k, \phi_k) d\Omega_{\mathbf{k}}$  being the  $l$ -wave pair state ( $l$  is an odd integer) [59]. As shown in Fig. 5(c),  $p$ -wave pair-



ing is dominant when  $n = 35$ . Importantly, new pairing states emerge when the FS is deformed strongly. As depicted in Fig. 5(d),  $f$ -wave ( $l = 3$ ) and  $h$ -wave ( $l = 5$ ) pairing, together with  $p$ -wave pairing, are found when  $n = 55$ . A systematic study shows that the population of the Cooper pairs can be enhanced by dressing to higher (more strongly interacting) Rydberg states. In Fig. 5(e), the total population of individual pair states,  $\bar{\Delta}_l = \int d^3\mathbf{k} \Delta_l(\mathbf{k})$ , is shown. When  $n$  increases, the occupation of  $p$ -,  $f$ -, and  $h$ -wave pairs also increases. In particular, considerable  $f$ - and  $h$ -wave populations are obtained when  $n > 40$ .

*Discussion and outlook.* The quantum simulation of  $p$ - and  $f$ -wave pairing with ultracold atoms has attracted much attention due to their importance in understanding superfluidity in  $^3\text{He-A}$  [51],  $^3\text{He-B}$  phase [52], and unconventional superconductors [53]. It has been shown that  $p$ -wave pairing can be realized with ultracold fermions with the dipolar interaction [21, 62–65] or isotropic dressed interaction in three dimensions [46]. However,  $f$ -wave pairing can only occur in 2D under extra restricted conditions, including Bose-Fermi mixed interactions [66, 67], excited bands [68], and repulsive Rydberg-dressed interactions [49, 50]. Our results show that an anisotropic Rydberg-dressed interaction allows to achieve such unconventional pairing states in three dimensions (3D). Moreover, it even provides access to the  $h$ -wave pairing channel.

Such  $h$ -wave pairing has not been thoroughly studied and is certainly worth further exploration. The anisotropic and

attractive dressed interaction opens further opportunities to probe novel phases, such as the nematic phase [2], topological superfluid [64, 69, 70], and supersolid phases [71, 72], as well as to probe nonequilibrium dynamics driven by long-range anisotropic interactions [45, 73]. Finally, we remark that anisotropic but repulsive interactions [55] can be obtained in the Rydberg dressing of  $^{39}\text{K}$  atoms [74]. Such repulsive interaction allows for probing the Kohn-Luttinger mechanism [75–77].

*Acknowledgments.* We are thankful for useful discussions with Yongqiang Li, Vijay Shenoy, S. Kumar Mallavarapu, and Gary McCormack. Y.Z. acknowledges support from National Natural Science Foundation of China (Grant No. 12088101) and NSAF (Grant No. U1930403). W.L. acknowledges support from the EPSRC through Grant No. EP/R04340X/1 via the QuantERA project “ERyQSenS”, the UKIERI-UGC Thematic Partnership (IND/CONT/G/16-17/73), and the Royal Society through the International Exchanges Cost Share Award No. IEC\NSFC\181078. R.N. acknowledges DST-SERB for Swarnajayanti Fellowship File No. SB/SJF/2020-21/19. I.L. acknowledges support from the “Wissenschaftler Rückkehrprogramm GSO/CZS” of the Carl-Zeiss-Stiftung and the German Scholars Organization e.V., as well as the Deutsche Forschungsgemeinschaft through SPP 1929 (GiRyd), Grant No. 428276754, and the “Internationale Spitzenforschung” program of the BW Foundation. We are grateful for access to the Augusta High Performance Computing Facility at the University of Nottingham.

- 
- [1] G. Baym and C. Pethick, *Landau Fermi-Liquid Theory: Concepts and Applications* (John Wiley & Sons, New York, 2008).
- [2] S. A. Kivelson, E. Fradkin, and V. J. Emery, Electronic liquid-crystal phases of a doped Mott insulator, *Nature (London)* **393**, 550 (1998).
- [3] I. I. Pomeranchuk, On the stability of a Fermi liquid, *Sov. Phys. JETP* **8**, 361 (1959).
- [4] S. Giorgini, L. P. Pitaevskii, and S. Stringari, Theory of ultracold atomic Fermi gases, *Rev. Mod. Phys.* **80**, 1215 (2008).
- [5] T. E. Drake, Y. Sagi, R. Paudel, J. T. Stewart, J. P. Gaebler, and D. S. Jin, Direct observation of the Fermi surface in an ultracold atomic gas, *Phys. Rev. A* **86**, 031601(R) (2012).
- [6] B. Mukherjee, Z. Yan, P. B. Patel, Z. Hadzibabic, T. Yefsah, J. Struck, and M. W. Zwierlein, Homogeneous atomic Fermi gases, *Phys. Rev. Lett.* **118**, 123401 (2017).
- [7] M. Marinescu and L. You, Controlling atom-atom interaction at ultralow temperatures by dc electric fields, *Phys. Rev. Lett.* **81**, 4596 (1998), publisher: American Physical Society.
- [8] K.-K. Ni, S. Ospelkaus, M. H. G. de Miranda, A. Pe’er, B. Neyenhuis, J. J. Zirbel, S. Kotochigova, P. S. Julienne, D. S. Jin, and J. Ye, A high phase-space-density gas of polar molecules, *Science* **322**, 231 (2008).
- [9] M. Lu, N. Q. Burdick, and B. L. Lev, Quantum degenerate dipolar Fermi gas, *Phys. Rev. Lett.* **108**, 215301 (2012).
- [10] M. A. Baranov, M. Dalmonte, G. Pupillo, and P. Zoller, Condensed matter theory of dipolar quantum gases, *Chem. Rev.* **112**, 5012 (2012).
- [11] T. Shi, S.-H. Zou, H. Hu, C.-P. Sun, and S. Yi, Ultracold Fermi gases with resonant dipole-dipole interaction, *Phys. Rev. Lett.* **110**, 045301 (2013).
- [12] S. Baier, D. Petter, J. H. Becher, A. Patscheider, G. Natale, L. Chomaz, M. J. Mark, and F. Ferlaino, Realization of a strongly interacting Fermi gas of dipolar atoms, *Phys. Rev. Lett.* **121**, 093602 (2018).
- [13] A. Trautmann, P. Ilzhöfer, G. Durastante, C. Politi, M. Sohmen, M. J. Mark, and F. Ferlaino, Dipolar quantum mixtures of erbium and dysprosium atoms, *Phys. Rev. Lett.* **121**, 213601 (2018).
- [14] T. Miyakawa, T. Sogo, and H. Pu, Phase-space deformation of a trapped dipolar Fermi gas, *Phys. Rev. A* **77**, 061603(R) (2008).
- [15] G. M. Bruun and E. Taylor, Quantum phases of a two-dimensional dipolar Fermi gas, *Phys. Rev. Lett.* **101**, 245301 (2008).
- [16] B. M. Fregoso and E. Fradkin, Ferronematic ground state of the dilute dipolar Fermi gas, *Phys. Rev. Lett.* **103**, 205301 (2009).
- [17] J.-N. Zhang and S. Yi, Fermi surface of a trapped dipolar Fermi gas, *Phys. Rev. A* **80**, 053614 (2009).
- [18] T. Sogo, L. He, T. Miyakawa, S. Yi, H. Lu, and H. Pu, Dynamical properties of dipolar Fermi gases, *New J. Phys.* **11**, 055017 (2009).
- [19] Y. Yamaguchi, T. Sogo, T. Ito, and T. Miyakawa, Density-wave instability in a two-dimensional dipolar Fermi gas, *Phys. Rev. A* **82**, 013643 (2010).
- [20] D. Baillie and P. B. Blakie, Thermodynamics and coherence of a trapped dipolar Fermi gas, *Phys. Rev. A* **82**, 033605 (2010).
- [21] C. Zhao, L. Jiang, X. Liu, W. M. Liu, X. Zou, and H. Pu, Hartree-Fock-Bogoliubov theory of dipolar Fermi gases, *Phys. Rev. A* **81**, 063642 (2010).
- [22] F. Wächtler, A. R. P. Lima, and A. Pelster, Low-lying excitation

- modes of trapped dipolar Fermi gases: From the collisionless to the hydrodynamic regime, *Phys. Rev. A* **96**, 043608 (2017).
- [23] K. Aikawa, S. Baier, A. Frisch, M. Mark, C. Ravensbergen, and F. Ferlaino, Observation of Fermi surface deformation in a dipolar quantum gas, *Science* **345**, 1484 (2014).
- [24] I. Bouchoule and K. Mølmer, Spin squeezing of atoms by the dipole interaction in virtually excited Rydberg states, *Phys. Rev. A* **65**, 041803(R) (2002).
- [25] N. Henkel, R. Nath, and T. Pohl, Three-dimensional roton excitations and supersolid formation in Rydberg-excited Bose-Einstein condensates, *Phys. Rev. Lett.* **104**, 195302 (2010).
- [26] G. Pupillo, A. Micheli, M. Boninsegni, I. Lesanovsky, and P. Zoller, Strongly correlated gases of Rydberg-dressed atoms: Quantum and classical dynamics, *Phys. Rev. Lett.* **104**, 223002 (2010).
- [27] J. Honer, H. Weimer, T. Pfau, and H. P. Büchler, Collective many-body interaction in Rydberg dressed atoms, *Phys. Rev. Lett.* **105**, 160404 (2010).
- [28] F. Cinti, P. Jain, M. Boninsegni, A. Micheli, P. Zoller, and G. Pupillo, Supersolid droplet crystal in a dipole-blockaded gas, *Phys. Rev. Lett.* **105**, 135301 (2010).
- [29] W. Li, L. Hamadeh, and I. Lesanovsky, Probing the interaction between Rydberg-dressed atoms through interference, *Phys. Rev. A* **85**, 053615 (2012).
- [30] M. Saffman, T. G. Walker, and K. Mølmer, Quantum information with Rydberg atoms, *Rev. Mod. Phys.* **82**, 2313 (2010).
- [31] E. Guardado-Sanchez, P. T. Brown, D. Mitra, T. Devakul, D. A. Huse, P. Schauf, and W. S. Bakr, Probing the quench dynamics of antiferromagnetic correlations in a 2D quantum Ising spin system, *Phys. Rev. X* **8**, 021069 (2018).
- [32] S. de Léséleuc, V. Lienhard, P. Scholl, D. Barredo, S. Weber, N. Lang, H. P. Büchler, T. Lahaye, and A. Browaeys, Observation of a symmetry-protected topological phase of interacting bosons with Rydberg atoms, *Science* **365**, 775 (2019).
- [33] A. W. Glaetzle, M. Dalmonte, R. Nath, C. Gross, I. Bloch, and P. Zoller, Designing frustrated quantum magnets with laser-dressed Rydberg atoms, *Phys. Rev. Lett.* **114**, 173002 (2015).
- [34] R. M. W. van Bijnen and T. Pohl, Quantum magnetism and topological ordering via Rydberg dressing near Förster resonances, *Phys. Rev. Lett.* **114**, 243002 (2015).
- [35] F. Cinti, T. Macrì, W. Lechner, G. Pupillo, and T. Pohl, Defect-induced supersolidity with soft-core bosons, *Nat. Commun.* **5**, 3235 (2014).
- [36] H. Schempp, G. Günter, S. Wüster, M. Weidemüller, and S. Whitlock, Correlated exciton transport in Rydberg-dressed-atom spin chains, *Phys. Rev. Lett.* **115**, 093002 (2015).
- [37] C.-H. Hsueh, C.-W. Wang, and W.-C. Wu, Vortex structures in a rotating Rydberg-dressed Bose-Einstein condensate with the Lee-Huang-Yang correction, *Phys. Rev. A* **102**, 063307 (2020).
- [38] Y. Zhou, Y. Li, R. Nath, and W. Li, Quench dynamics of Rydberg-dressed bosons on two-dimensional square lattices, *Phys. Rev. A* **101**, 013427 (2020).
- [39] J. Zeiher, R. van Bijnen, P. Schauf, S. Hild, J.-y. Choi, T. Pohl, I. Bloch, and C. Gross, Many-body interferometry of a Rydberg-dressed spin lattice, *Nat. Phys.* **12**, 1095 (2016).
- [40] J. Zeiher, J.-y. Choi, A. Rubio-Abadal, T. Pohl, R. van Bijnen, I. Bloch, and C. Gross, Coherent many-body spin dynamics in a long-range interacting Ising chain, *Phys. Rev. X* **7**, 041063 (2017).
- [41] V. Borish, O. Marković, J. A. Hines, S. V. Rajagopal, and M. Schleier-Smith, Transverse-field Ising dynamics in a Rydberg-dressed atomic gas, *Phys. Rev. Lett.* **124**, 063601 (2020).
- [42] Y. Li, A. Geißler, W. Hofstetter, and W. Li, Supersolidity of lattice bosons immersed in strongly correlated Rydberg dressed atoms, *Phys. Rev. A* **97**, 023619 (2018).
- [43] R. Mukherjee, C. Ates, W. Li, and S. Wüster, Phase-imprinting of Bose-Einstein condensates with Rydberg impurities, *Phys. Rev. Lett.* **115**, 040401 (2015).
- [44] Y. Li, H. Cai, D.-w. Wang, L. Li, J. Yuan, and W. Li, Many-body chiral edge currents and sliding phases of atomic spin waves in momentum-space lattice, *Phys. Rev. Lett.* **124**, 140401 (2020).
- [45] E. Guardado-Sanchez, B. M. Spar, P. Schauss, R. Belyansky, J. T. Young, P. Bienias, A. V. Gorshkov, T. Iadecola, and W. S. Bakr, Quench dynamics of a fermi gas with strong nonlocal interactions, *Phys. Rev. X* **11**, 021036 (2021).
- [46] B. Xiong, H. H. Jen, and D.-W. Wang, Topological superfluid by blockade effects in a Rydberg-dressed Fermi gas, *Phys. Rev. A* **90**, 013631 (2014).
- [47] X. Li and S. D. Sarma, Exotic topological density waves in cold atomic Rydberg-dressed fermions, *Nat. Commun.* **6**, 7137 (2015).
- [48] W.-H. Li, T.-C. Hsieh, C.-Y. Mou, and D.-W. Wang, Emergence of a metallic quantum solid phase in a Rydberg-dressed Fermi gas, *Phys. Rev. Lett.* **117**, 035301 (2016).
- [49] R. Khassseh, S. H. Abedinpour, and B. Tanatar, Phase diagram and dynamics of Rydberg-dressed fermions in two dimensions, *Phys. Rev. A* **96**, 053611 (2017).
- [50] A. Keleş, E. Zhao, and X. Li,  $f$ -wave superfluidity from repulsive interaction in Rydberg-dressed Fermi gas, *Phys. Rev. A* **101**, 023624 (2020).
- [51] U. E. Israelsson, B. C. Crooker, H. M. Bozler, and C. M. Gould,  $f$ -wave effects in superfluid  $^3\text{He-A}$ , *Phys. Rev. Lett.* **56**, 2383 (1986).
- [52] J. P. Davis, J. Pollanen, H. Choi, J. A. Sauls, and W. P. Halperin, Discovery of an excited pair state in superfluid  $^3\text{He}$ , *Nat. Phys.* **4**, 571 (2008).
- [53] G. R. Stewart, Unconventional superconductivity, *Adv. Phys.* **66**, 75 (2017).
- [54] A. A. Kamenski, N. L. Manakov, S. N. Mokhnenko, and V. D. Ovsiannikov, Energy of van der Waals and dipole-dipole interactions between atoms in Rydberg states, *Phys. Rev. A* **96**, 032716 (2017).
- [55] See the Supplemental Material for additional details on the van der Waals interaction and HFB approximation, which also includes Refs. 56, 78–82.
- [56] J. E. Johnson and S. L. Rolston, Interactions between Rydberg-dressed atoms, *Phys. Rev. A* **82**, 033412 (2010), 1006.3212.
- [57] C. Cohen-Tannoudji, J. Dupont-Roc, and G. Grynberg, Nonperturbative calculation of transition amplitudes, in *Atom-Photon Interactions: Basic Process and Applications* (John Wiley & Sons, New York, 1998), Chap. 3, pp. 165–255.
- [58] P. Ring and P. Schuck, *The Nuclear Many-Body Problem* (Springer-Verlag, Berlin, 1980).
- [59] L. You and M. Marinescu, Prospects for  $p$ -wave paired Bardeen-Cooper-Schrieffer states of fermionic atoms, *Phys. Rev. A* **60**, 2324 (1999).
- [60] C.-K. Chan, C. Wu, W.-C. Lee, and S. Das Sarma, Anisotropic-Fermi-liquid theory of ultracold fermionic polar molecules: Landau parameters and collective modes, *Phys. Rev. A* **81**, 023602 (2010).
- [61] S. Ronen and J. L. Bohn, Zero sound in dipolar Fermi gases, *Phys. Rev. A* **81**, 033601 (2010).
- [62] T.-L. Ho and R. B. Diener, Fermion superfluids of nonzero orbital angular momentum near resonance, *Phys. Rev. Lett.* **94**, 090402 (2005).
- [63] C.-H. Cheng and S.-K. Yip, Pairing symmetry in an anisotropic Fermi superfluid under a  $p$ -wave Feshbach resonance, *Phys. Rev.*

- B **73**, 064517 (2006).
- [64] N. R. Cooper and G. V. Shlyapnikov, Stable topological superfluid phase of ultracold polar fermionic molecules, *Phys. Rev. Lett.* **103**, 155302 (2009).
- [65] A. K. Fedorov, S. I. Matveenko, V. I. Yudson, and G. V. Shlyapnikov, Novel  $p$ -wave superfluids of fermionic polar molecules, *Sci. Rep.* **6**, 27448 (2016).
- [66] W.-C. Lee, C. Wu, and S. Das Sarma,  $f$ -wave pairing of cold atoms in optical lattices, *Phys. Rev. A* **82**, 053611 (2010).
- [67] L. Mathey, S.-W. Tsai, and A. H. Castro Neto, Exotic superconducting phases of ultracold atom mixtures on triangular lattices, *Phys. Rev. B* **75**, 174516 (2007).
- [68] H.-H. Hung, W.-C. Lee, and C. Wu, Frustrated Cooper pairing and  $f$ -wave supersolidity in cold-atom optical lattices, *Phys. Rev. B* **83**, 144506 (2011).
- [69] B. Liu and L. Yin, Topological  $p_x + ip_y$  superfluid phase of a dipolar Fermi gas in a two-dimensional optical lattice, *Phys. Rev. A* **86**, 031603(R) (2012).
- [70] B. Liu, X. Li, L. Yin, and W. V. Liu, Weyl superfluidity in a three-dimensional dipolar Fermi gas, *Phys. Rev. Lett.* **114**, 045302 (2015).
- [71] A.-L. Gadsbølle and G. M. Bruun, Harmonically trapped dipolar fermions in a two-dimensional square lattice, *Phys. Rev. A* **85**, 021604(R) (2012).
- [72] T.-S. Zeng and L. Yin, Supersolidity of a dipolar Fermi gas in a cubic optical lattice, *Phys. Rev. B* **89**, 174511 (2014).
- [73] N. Nessi, A. Iucci, and M. A. Cazalilla, Quantum quench and prethermalization dynamics in a two-dimensional Fermi gas with long-range interactions, *Phys. Rev. Lett.* **113**, 210402 (2014).
- [74] A. Arias, G. Lochead, T. M. Wintermantel, S. Helmrich, and S. Whitlock, Realization of a Rydberg-dressed Ramsey interferometer and electrometer, *Phys. Rev. Lett.* **122**, 053601 (2019).
- [75] D. Shechtman, I. Blech, D. Gratias, and J. W. Cahn, Metallic phase with long-range orientational order and no translational symmetry, *Phys. Rev. Lett.* **53**, 1951 (1984).
- [76] S. Maiti and A. V. Chubukov, Superconductivity from repulsive interaction, in *Lectures on the Physics of Strongly Correlated Systems XVII: Seventeenth Training Course in the Physics of Strongly Correlated Systems*, edited by A. Avella and F. Mancini, *AIP Conf. Proc.* **1550** (AIP, New York, 2013), p. 3.
- [77] Y. Cao, Y. Zhang, Y.-B. Liu, C.-C. Liu, W.-Q. Chen, and F. Yang, Kohn-Luttinger mechanism driven exotic topological superconductivity on the Penrose lattice, *Phys. Rev. Lett.* **125**, 017002 (2020).
- [78] N. Šibalić, J. Pritchard, C. Adams, and K. Weatherill, ARC: An open-source library for calculating properties of alkali Rydberg atoms, *Comput. Phys. Commun.* **220**, 319 (2017).
- [79] E. Robertson, N. Šibalić, R. Potvliege, and M. Jones, ARC 3.0: An expanded PYTHON toolbox for atomic physics calculations, *Comput. Phys. Commun.* **261**, 107814 (2021).
- [80] Z. Lan, J. Minář, E. Levi, W. Li, and I. Lesanovsky, Emergent devil's staircase without particle-hole symmetry in Rydberg quantum gases with competing attractive and repulsive interactions, *Phys. Rev. Lett.* **115**, 203001 (2015).
- [81] Z. Lan, I. Lesanovsky, and W. Li, Devil's staircases without particle-hole symmetry, *Phys. Rev. B* **97**, 075117 (2018).
- [82] N. D. Woods, M. C. Payne, and P. J. Hasnip, Computing the self-consistent field in Kohn-Sham density functional theory, *J. Phys. Condens. Matter* **31**, 453001 (2019).

# Supplementary material for: Multipolar Fermi-surface deformation in a Rydberg-dressed Fermi gas with long-range anisotropic interactions

Yijia Zhou<sup>1,2</sup>, Rejish Nath<sup>3</sup>, Haibin Wu<sup>4,5</sup>, Igor Lesanovsky<sup>1,6</sup>, Weibin Li<sup>1</sup>

<sup>1</sup>*School of Physics and Astronomy and Centre for the Mathematics and Theoretical Physics of Quantum Non-equilibrium Systems, University of Nottingham, Nottingham, NG7 2RD, UK*

<sup>2</sup>*Graduate School of China Academy of Engineering Physics, Beijing, 100193, China*

<sup>3</sup>*Department of Physics, Indian Institute of Science Education and Research, Dr. Homi Bhabha Road, Pune- 411008, Maharashtra, India*

<sup>4</sup>*State Key Laboratory of Precision Spectroscopy, East China Normal University, Shanghai 200062, China*

<sup>5</sup>*Collaborative Innovation Center of Extreme Optics, Shanxi University, Taiyuan 030006, China*

<sup>6</sup>*Institut für Theoretische Physik, University of Tübingen, 72076 Tübingen, Germany*

This supplementary material gives details on the analysis in the main text and provides additional data for calculating the dressed interaction potential.

## I. DISPERSION COEFFICIENTS OF THE RYDBERG STATES

The dispersion coefficient  $C_6(\theta)$  is calculated with the Alkali-Rydberg-Calculator (ARC) package [S1, S2]. In the Rydberg  $|nD_{5/2}\rangle$  state, the van der Waals interaction is cylindrically symmetric, i.e.  $C_6(\theta)$  is dependent on the polar angle  $\theta$  but not on the azimuth angle  $\phi$ . In the Rydberg-dressing, one would like to gain strong soft-core interactions while maintaining a small excitation in the Rydberg state, whose population is approximately given by  $\Omega^2/4\delta^2$ . In a recent Rydberg dressing experiment with <sup>6</sup>Li atoms, it was shown that relatively strong interactions can be achieved with  $\Omega \lesssim 0.3\delta$  [S3]. In our simulation, we consider parameters  $\Omega \approx 0.15\delta$  throughout. Furthermore, coefficient  $C_6(\theta)$  should have same sign for all  $\theta$  in order to avoid resonances [S4, S5]. Our calculations show that this is always guaranteed for <sup>6</sup>Li.

The anisotropy of the Rydberg atom interaction depends on the angular momentum quantum number of the Rydberg state. In  $nS$  states, the anisotropy is typically negligible. In order to find the maximal anisotropic interacting states, we have examined both the  $nP$  and  $nD$  states. The ratio of  $C_6(\theta)$  at  $\theta = 0$  and  $\pi/2$  is used to quantify the strength of the anisotropy. Strong anisotropic interactions will be obtained when the ratio is much larger or smaller than 1. As shown in Fig. S1, we found that the most anisotropic interaction appears in  $nD_{5/2}$  states with  $m_j = 5/2$ , where  $C_6(0)/C_6(\pi/2) \approx 0.17$ . Therefore we will focus on  $|nD_{5/2}, m_j = 5/2\rangle$  states of <sup>6</sup>Li atoms in the following discussion. Another important feature here is that this ratio is not sensitive to the principal quantum number  $n$  for <sup>6</sup>Li atoms. In contrast, the anisotropy of <sup>40</sup>K atoms varies strongly when varying  $n$ , see Fig. S1(b). In  $|nP_{3/2}\rangle$  states, we find repulsive interactions between Rydberg atoms, i.e.  $C(\theta) > 0$ . This state can be used to create anisotropic and repulsive dressed interactions with <sup>40</sup>K atoms.

The angular dependent coefficient  $C_6(\theta)$  can be expressed in the following form [S6],

$$C_6(\theta) = R_{ss} - \frac{m_j^2(3\cos^2\theta - 2)}{12J^2}R_{aa} + \frac{3m_j^2 - J(J+1)(3\cos^2\theta - 1)}{2J(2J-1)}R_{sT} + \frac{3}{2} \left[ \frac{3m_j^2 - J(J+1)}{2J(2J-1)} \right]^2 (9\cos^4\theta - 8\cos^2\theta)R_{TT}, \quad (\text{S1})$$

where the coefficients  $R_{ss}$ ,  $R_{aa}$ ,  $R_{sT}$  and  $R_{TT}$  are irreducible components of the van der Waals coefficient, and are called scalar, axial, scalar-tensor and tensor-tensor components, respectively. Their numerical values are shown in Fig. S2. These data can be fitted with the power-law form, given by  $[-3.4824, -24.1858, 0.3262, 0.0135] \times 10^{-17}n^{11}$  GHz  $\mu\text{m}^6$ .

Due to the cylindrical symmetry of the van der Waals interaction, we can express  $C(\theta)$  in terms of spherical harmonics  $Y_{l0}(\theta, \phi)$ ,

$$C_6(\theta) = C_0Y_{00}(\theta, \phi) + C_2Y_{20}(\theta, \phi) + C_4Y_{40}(\theta, \phi), \quad (\text{S2})$$



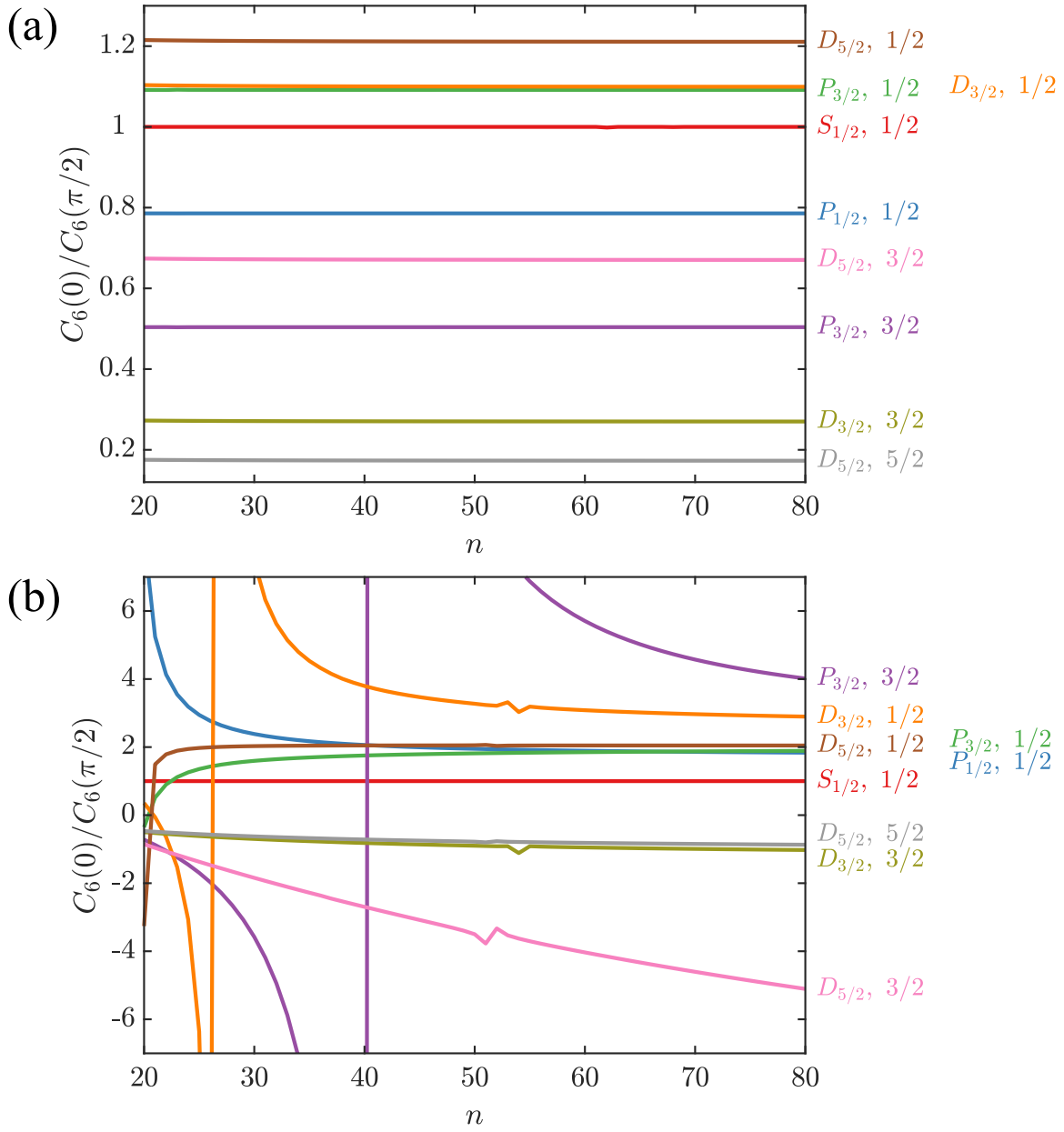


FIG. S1. Ratio  $C_6(0)/C_6(\pi/2)$  for various Rydberg states of (a)  ${}^6\text{Li}$  and (b)  ${}^{40}\text{K}$  atoms. (a) For  ${}^6\text{Li}$ , the van der Waals interaction is the most anisotropic in  $|nD_{5/2}, m_j = 5/2\rangle$  state, and its anisotropy  $C_6(0)/C_6(\pi/2) \approx 0.173$  is largely insensitive to the principal quantum number  $n$ . (b) For  ${}^{40}\text{K}$ , the sign of  $C_6(\pi/2)$  flips at  $n = 40 \rightarrow 41$  for  $|P_{3/2}, m_j = 3/2\rangle$ , and  $n = 26 \rightarrow 27$  for  $|D_{3/2}, m_j = 1/2\rangle$ . This means that the ratio near the resonant states is particularly large. For example, At  $|41P_{3/2}, m_j = 3/2\rangle$ ,  $C_6(0)/C_6(\pi/2) \approx 261$ , and At  $|27D_{3/2}, m_j = 1/2\rangle$ ,  $C_6(0)/C_6(\pi/2) \approx 63$ .

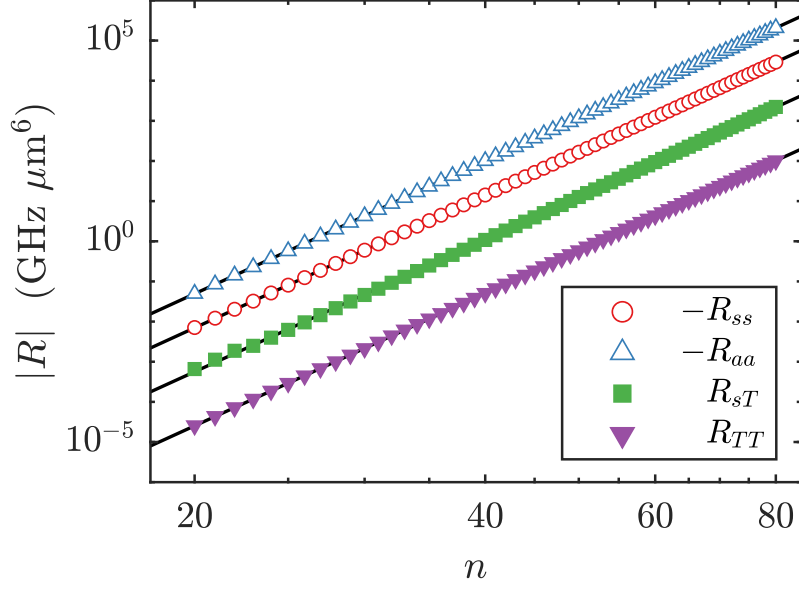


FIG. S2. (a) Irreducible components for  $C_6$  parameters of  ${}^6\text{Li}$  in  $nD_{5/2}$  states.  $R_{ss}$  is for the scalar component,  $R_{aa}$  is for the axial component,  $R_{sT}$  is for the scalar-tensor component, and  $R_{TT}$  is for the tensor-tensor component. Each component is fitted by  $R \sim n^{11}$  (solid lines).

where we have defined parameters  $C_j$  ( $j = 0, 2, 4$ ),

$$\begin{aligned}
 C_0 &= 2\sqrt{\pi}R_{ss} + \frac{m_j^2}{6J^2}\sqrt{\pi}R_{aa} + \frac{3m_j^2}{J(2J-1)}\sqrt{\pi}R_{sT} - \frac{13}{5}\left[\frac{3m_j^2 - J(J+1)}{2J(2J-1)}\right]^2\sqrt{\pi}R_{TT}, \\
 C_2 &= -\sqrt{\frac{\pi}{5}}\frac{m_j^2}{3J^2}R_{aa} - \sqrt{\frac{\pi}{5}}\frac{2J+2}{2J-1}R_{sT} + \sqrt{\frac{\pi}{5}}\frac{4}{9}\left[\frac{3m_j^2 - J(J+1)}{2J(2J-1)}\right]^2R_{TT}, \\
 C_4 &= \frac{72\sqrt{\pi}}{35}\left[\frac{3m_j^2 - J(J+1)}{2J(2J-1)}\right]^2R_{TT}.
 \end{aligned} \tag{S3}$$

In the above expression  $m_j = 0$  due to the cylindrical symmetry, which means there is no dependence on azimuth angle  $\phi$  in the spherical harmonics. For the sake of simplicity, we rewrite  $Y_{10}(\theta, \phi) \equiv Y_{10}(\theta)$ .

## II. DETAILS ON THE HARTREE-FOCK-BOGOLIUBOV APPROXIMATION

The Hamiltonian in momentum space

$$H = \int \frac{d^3\mathbf{k}}{(2\pi)^3} \frac{|\mathbf{k}|^2}{2m} \hat{a}_{\mathbf{k}}^\dagger \hat{a}_{\mathbf{k}} + \iiint \frac{d^3\mathbf{k}}{(2\pi)^3} \frac{d^3\mathbf{k}'}{(2\pi)^3} \frac{d^3\mathbf{q}}{(2\pi)^3} \hat{a}_{\mathbf{k}+\mathbf{q}}^\dagger \hat{a}_{\mathbf{k}'}^\dagger \tilde{V}(\mathbf{q}) \hat{a}_{\mathbf{k}'+\mathbf{q}} \hat{a}_{\mathbf{k}}, \tag{S4}$$

where  $\tilde{V}(\mathbf{q})$  is the Fourier transform of the two-body interaction potential  $V(\mathbf{r})$ . According to the mean-field theory, the four-operator term is reduced to

$$\begin{aligned}
 \hat{a}_{\mathbf{k}+\mathbf{q}}^\dagger \hat{a}_{\mathbf{k}}^\dagger \hat{a}_{\mathbf{k}'+\mathbf{q}} \hat{a}_{\mathbf{k}} &\approx \langle \hat{a}_{\mathbf{k}+\mathbf{q}}^\dagger \hat{a}_{\mathbf{k}} \rangle \hat{a}_{\mathbf{k}'}^\dagger \hat{a}_{\mathbf{k}'+\mathbf{q}} + \langle \hat{a}_{\mathbf{k}'}^\dagger \hat{a}_{\mathbf{k}'+\mathbf{q}} \rangle \hat{a}_{\mathbf{k}+\mathbf{q}}^\dagger \hat{a}_{\mathbf{k}} \\
 &\quad - \langle \hat{a}_{\mathbf{k}+\mathbf{q}}^\dagger \hat{a}_{\mathbf{k}'+\mathbf{q}} \rangle \hat{a}_{\mathbf{k}'}^\dagger \hat{a}_{\mathbf{k}} - \langle \hat{a}_{\mathbf{k}'}^\dagger \hat{a}_{\mathbf{k}} \rangle \hat{a}_{\mathbf{k}+\mathbf{q}}^\dagger \hat{a}_{\mathbf{k}'+\mathbf{q}} \\
 &\quad + \langle \hat{a}_{\mathbf{k}+\mathbf{q}}^\dagger \hat{a}_{\mathbf{k}'}^\dagger \rangle \hat{a}_{\mathbf{k}'+\mathbf{q}} \hat{a}_{\mathbf{k}} + \langle \hat{a}_{\mathbf{k}'+\mathbf{q}} \hat{a}_{\mathbf{k}} \rangle \hat{a}_{\mathbf{k}+\mathbf{q}}^\dagger \hat{a}_{\mathbf{k}'}^\dagger.
 \end{aligned}$$

The first line of the right hand side gives the Hartree direct energy with  $\mathbf{q} = 0$ . The second line accounts for the Fock exchange energy, with  $\mathbf{k} = \mathbf{k}'$ . The third line is the Bogoliubov term, with  $\mathbf{k} + \mathbf{q} = -\mathbf{k}'$ . With the above approximation, we obtain the

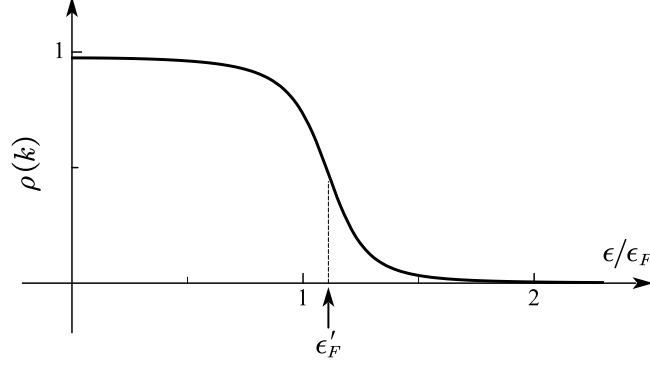


FIG. S3. Demonstration of the fitting of the FS. The fitting parameter  $\epsilon'_F$  indicates the energy where the slope of  $\rho(k)$  is largest. In this demonstration, the parameters are  $\epsilon'_F = 1.1\epsilon_F$  and  $\Delta'_F = 0.2\epsilon_F$ .

Hartree-Fock-Bogoliubov (HFB) Hamiltonian,

$$H = \int \frac{d^3\mathbf{k}}{(2\pi)^3} \left\{ \left[ \frac{|\mathbf{k}|^2}{2m} + U_d + U_e(\mathbf{k}) \right] \left( \hat{a}_{\mathbf{k}}^\dagger \hat{a}_{\mathbf{k}} + \hat{a}_{-\mathbf{k}}^\dagger \hat{a}_{-\mathbf{k}} \right) + \Delta(\mathbf{k}) \hat{a}_{\mathbf{k}}^\dagger \hat{a}_{-\mathbf{k}}^\dagger + \Delta^*(\mathbf{k}) \hat{a}_{-\mathbf{k}} \hat{a}_{\mathbf{k}} \right\}, \quad (\text{S5})$$

where we have defined,

$$\begin{aligned} U_d &= N\tilde{V}(0), \\ U_e(\mathbf{k}) &= - \int \frac{d^3\mathbf{k}'}{(2\pi)^3} \tilde{V}(\mathbf{k} - \mathbf{k}') \langle \hat{a}_{\mathbf{k}'}^\dagger \hat{a}_{\mathbf{k}'} \rangle, \\ \Delta(\mathbf{k}) &= \int \frac{d^3\mathbf{k}'}{(2\pi)^3} \tilde{V}(\mathbf{k} - \mathbf{k}') \langle \hat{a}_{-\mathbf{k}'} \hat{a}_{\mathbf{k}'} \rangle, \end{aligned}$$

and  $N = \int d^3\mathbf{k}/(2\pi)^3 \langle \hat{a}_{\mathbf{k}}^\dagger \hat{a}_{\mathbf{k}} \rangle$  is the number of particles. The Hartree term,  $U_d$ , is a constant, and can be absorbed into the chemical potential  $\mu$  in a grand canonical ensemble. The Fock term,  $U_e(\mathbf{k})$ , can modify the kinetic energy. When  $U_e(\mathbf{k})$  is anisotropic, it can modify symmetry of the FS. The gap function  $\Delta(\mathbf{k})$  gives the BCS order parameter. It also reveals the Fermi surface instability due to the formation of Cooper pairs. It is antisymmetric with respect to momentum  $\mathbf{k}$ , i.e.  $\Delta(\mathbf{k}) = -\Delta(-\mathbf{k})$ . By letting  $\Delta_{\mathbf{k}} = 0$ , one returns to the Hartree-Fock (HF) approximation, where the Fermi surface is well defined by solving  $\mu = |\mathbf{k}|^2/(2m) + U_e(\mathbf{k})$ .

With the BCS wave function  $|G\rangle_{\text{BCS}} = \prod_{\mathbf{k}} \left( u_{\mathbf{k}} + v_{\mathbf{k}} \hat{a}_{\mathbf{k}}^\dagger \hat{a}_{-\mathbf{k}}^\dagger \right) |0\rangle$ , it can be found that  $\langle \hat{a}_{\mathbf{k}}^\dagger \hat{a}_{\mathbf{k}} \rangle = \tilde{\rho}(\mathbf{k}) = |v_{\mathbf{k}}|^2$ , and  $\langle \hat{a}_{-\mathbf{k}} \hat{a}_{\mathbf{k}} \rangle = u_{\mathbf{k}}^* v_{\mathbf{k}}$ . The solution to  $(u_{\mathbf{k}}, v_{\mathbf{k}})$  and the self-consistent gap equation reads

$$u_{\mathbf{k}}^2 = \frac{1}{2} \left( 1 + \frac{\xi_{\mathbf{k}}}{\sqrt{\xi_{\mathbf{k}}^2 + |\Delta_{\mathbf{k}}|^2}} \right), \quad v_{\mathbf{k}}^2 = \frac{1}{2} \left( 1 - \frac{\xi_{\mathbf{k}}}{\sqrt{\xi_{\mathbf{k}}^2 + |\Delta_{\mathbf{k}}|^2}} \right), \quad (\text{S6})$$

$$\Delta_{\mathbf{k}} = \int \frac{d^3\mathbf{k}'}{(2\pi)^3} \tilde{V}(\mathbf{k} - \mathbf{k}') \frac{\Delta_{\mathbf{k}'}}{\sqrt{\xi_{\mathbf{k}'}^2 + |\Delta_{\mathbf{k}'}|^2}}, \quad (\text{S7})$$

where  $\xi_{\mathbf{k}} = |\mathbf{k}|^2/(2m) + U_e(\mathbf{k}) - \mu$ . The deformation of the FS is associated with the formation of Cooper pairs, which can be quantified by the pair density  $\rho_p = \sum_{\mathbf{k}} u_{\mathbf{k}}^2 v_{\mathbf{k}}^2$ .

The numerical solutions to the momentum density  $\tilde{\rho}(\mathbf{k})$  and the order parameter  $\Delta(\mathbf{k})$  are obtained by the self-consistent iteration with the Krasnosel'ski-Mann algorithm [S7]. For each iteration step,  $\tilde{\rho}(\mathbf{k})$  and  $\Delta(\mathbf{k})$  are updated by Eq. (S6)-(S7), and then the new solution is damped by the old one, such that  $\tilde{\rho}(\mathbf{k})^{\text{new}} = \tilde{\rho}(\mathbf{k})^{\text{new}} + \eta[\tilde{\rho}(\mathbf{k})^{\text{old}} - \tilde{\rho}(\mathbf{k})^{\text{new}}]$ . In practice we have used  $\eta = 0.5$  in the iteration, which provides an efficient way to carry out the numerical simulation. The same iteration procedure is applied to the gap function  $\Delta(\mathbf{k})$ .

### III. FITTING THE FERMI SURFACE

In the HFB approximation, the density distribution is depleted, see Fig. (2) in the main text. Here we employ a fitting procedure to approximately identify the FS [S8]. With the numerical solution of the momentum distribution, we fit the distribution with

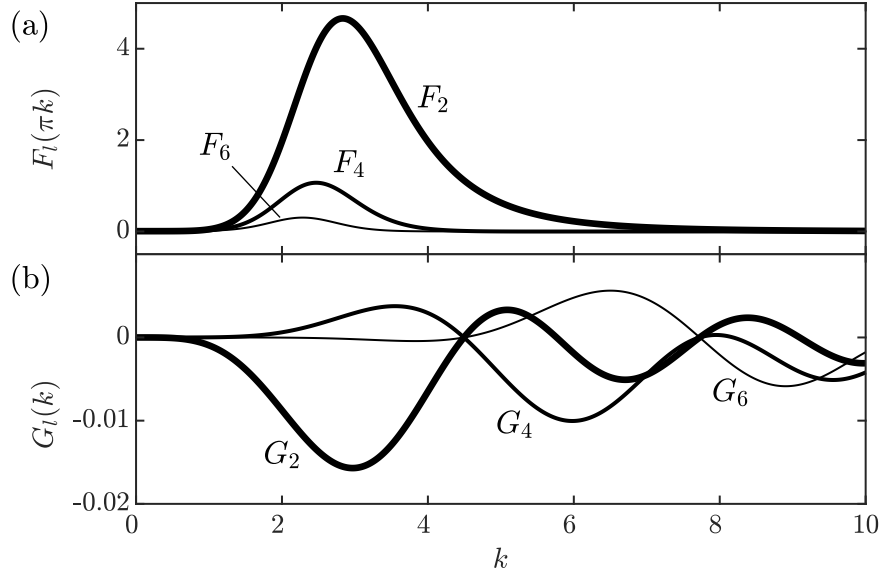


FIG. S4. (a) Function  $F_l(k)$  has a single peak. For larger  $l$ , the location of the peak moves towards to lower  $k$ . (b) Function  $G_l(k)$  oscillates with  $k$ . Increasing  $k$ , the amplitude of function  $G_l(k)$  decreases slowly.

the following function [S8]

$$\rho(k, \theta_k) = \frac{1}{2} \left( 1 - \frac{\epsilon_k - \epsilon'_F(\theta_k)}{\sqrt{[\epsilon_k - \epsilon'_F(\theta_k)]^2 + \Delta'(\theta_k)^2}} \right), \quad (\text{S8})$$

where  $\epsilon'_F(\theta_k)$  and  $\Delta'(\theta_k)$  are angular dependent fitting parameters. The parameter  $\epsilon'_F(\theta_k) = [k'_F(\theta_k)]^2/2m$  is used to approximately identify the FS, even though the FS is not well-defined. In Fig. S3, we demonstrate the location of the approximate FS. It shows that parameter  $\epsilon'_F(\theta_k)$  gives roughly the largest slope of the density distribution.

#### IV. THE PROJECTION COEFFICIENT

##### A. Density distribution and the projection coefficient

In the main text, we showed that the geometry of the deformed FS can be characterized by the projection coefficient  $\lambda_l$ . Here we illustrate how one can obtain the projection coefficient from the density distribution  $\rho(\mathbf{k})$  within the Hartree-Fock approximation. Neglecting the depletion, the density distribution is described approximately  $\tilde{\rho}'(\mathbf{k}) = \Theta(k_F + \delta k_F(\theta_k) - |\mathbf{k}|)$ . The anisotropy of the approximate FS is characterized by  $\delta k_F(\theta_k)$ . We then project the density distribution  $\tilde{\rho}'(\mathbf{k})$  to the spherical



harmonics,

$$\begin{aligned}
\lambda_l^{\text{HF}} &= \frac{1}{\rho} \int \frac{d^3\mathbf{k}}{(2\pi)^3} \tilde{\rho}'(\mathbf{k}) Y_{l0}(\theta_k, 0), \text{ for } l > 0 \\
&= \frac{1}{k_F^3/(6\pi^2)} \iint \frac{k^2 dk d\Omega_k}{(2\pi)^3} \Theta(k_F + \delta k_F - k(\theta_k)) Y_{l0}(\theta_k, 0) \\
&= \frac{3}{4\pi k_F^3} \int d\Omega_k \int_0^{k_F + \delta k_F(\theta_k)} k^2 dk Y_{l0}(\theta_k, 0) \\
&= \frac{1}{4\pi k_F^3} \int d\Omega_k [k_F + \delta k_F(\theta_k)]^3 Y_{l0}(\theta_k, 0) \\
&\approx \frac{1}{4\pi} \int d\Omega_k \left( 1 + 3 \frac{\delta k_F(\theta_k)}{k_F} \right) Y_{l0}(\theta_k, 0) \\
&\approx \frac{3}{4\pi} \int d\Omega_k \sum_{l'} \frac{1}{2E_F} \lambda'_{l'} Y_{l'0}(\theta_k, 0) Y_{l0}(\theta_k, 0) \\
&\approx \frac{3}{8\pi} \frac{\lambda'_l}{E_F}.
\end{aligned}$$

Here  $\lambda'_l$  is introduced as we directly expand  $\delta k_F$ ,

$$\frac{\delta k_F(\theta_k)}{k_F} = \frac{1}{2E_F} \sum_l \lambda'_l Y_{l0}(\theta_k, 0). \quad (\text{S9})$$

The above calculation establishes the relation between  $\lambda_l^{\text{HF}}$  with  $\lambda'_l$ . Note that the zeroth term  $\lambda_0 = \sqrt{\frac{1}{4\pi}}$  characterizes the spherical FS, and hence makes no contribution to the FS deformation.

Same derivation can be carried to calculate the projection coefficient with the density distribution  $\tilde{\rho}(\mathbf{k})$  obtained from the HBF calculation as follows,

$$\lambda_l = \frac{1}{\rho} \int \frac{d^3\mathbf{k}}{(2\pi)^3} \tilde{\rho}(\mathbf{k}) Y_{l0}(\theta_k, 0) = \frac{2\pi}{\rho} \int_0^\infty dk_z \int_0^\infty dk_x k_x \tilde{\rho}(k_x, k_z) Y_{l0} \left( \arctan \frac{k_x}{k_z}, 0 \right), \quad (\text{S10})$$

where  $\int dk_z$  and  $\int dk_x$  can be evaluated using the trapezoidal integration method. Similar to the perturbation calculation shown above, one finds the relation,  $\lambda_l = \frac{3}{8\pi} \frac{\lambda'_l}{E_F}$  ( $l > 0$ ), where  $\lambda_l$  is shown in Fig. 3 in the main text.

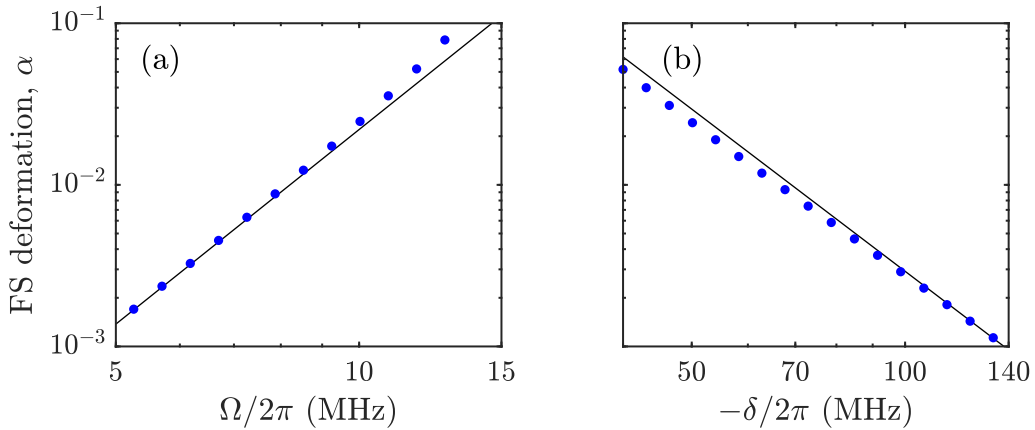


FIG. S5. Scaling relations of the Fermi surface deformation  $\alpha$  with respect to (a)  $\Omega$  and (b)  $\delta$ . The quantum number  $n = 32$  and the initial Fermi vector  $k_F = 2 \mu\text{m}^{-1}$ , which corresponds to  $\bar{R} = 1.77 \mu\text{m}$  and  $\rho = 1.35 \times 10^{11} \text{cm}^{-3}$ .

## B. Analysis of the projection coefficient in the perturbative calculation

We now turn to the discussion on the projection coefficient  $\lambda_l$ . As shown in the main text, the perturbed Fermi surface is given by the convolution of the interaction  $\tilde{V}(\mathbf{k})$  and the initial density distribution of the non-interacting Fermi gas,  $\tilde{\rho}_0(\mathbf{k}) = \Theta(k_F - |\mathbf{k}|)$ ,

$$\begin{aligned}
\frac{\delta \mathbf{k}_F}{k_F} &= \frac{1}{2E_F} \int \frac{d^3 \mathbf{q}}{(2\pi)^3} \tilde{V}(\mathbf{k}_F - \mathbf{q}) \tilde{\rho}_0(\mathbf{q}) = \frac{1}{2E_F} \int d^3 \mathbf{r} e^{i\mathbf{k} \cdot \mathbf{r}} V(\mathbf{r}) \rho_0^{\text{inv}}(\mathbf{r}) \\
&= \frac{1}{2E_F} \int r^2 \sin \theta dr d\theta d\phi V(r, \theta) \rho_0^{\text{inv}}(r) \sum_{l=0,1,2,\dots} 4\pi i^l j_l(|\mathbf{k}|r) \sum_{m=-l}^l Y_l^m(\theta, \phi) Y_l^{m*}(\theta_k, \phi_k) \\
&= \frac{1}{2E_F} \sum_{l=0,2,\dots} \int r^2 dr \left( 8\pi^2 \int \sin \theta d\theta V(r, \theta) Y_{l0}(\theta) \right) \rho_0^{\text{inv}}(|\mathbf{k}|r) i^l j_l(|\mathbf{k}|r) Y_{l0}(\theta_k) \\
&= \frac{1}{2E_F} \sum_{l=0,2,\dots} Y_{l0}(\theta_k) \int dk F_l[k/(k_F \bar{R})] G_l(k) \\
&= \frac{1}{2E_F} \sum_{l=0,2,\dots} \lambda'_l(k_F \bar{R}) Y_{l0}(\theta_k), \tag{S11}
\end{aligned}$$

where  $\rho_0^{\text{inv}}(r) = (2\pi^2)^{-1} j_1(k_F r)$  is the inverse Fourier transform of  $\tilde{\rho}_0(k)$ . The dimensionless functions  $F_l(k)$  and  $G_l(k)$  are defined by

$$F_l(k) = 8\pi^2 \int_0^\infty \sin \theta d\theta \frac{C_6(\theta)/(2\delta \bar{R}^6)}{C_6(\theta)/(2\delta \bar{R}^6) + k^6} Y_{l0}(\theta), \tag{S12a}$$

$$G_l(k) = i^l \rho_0^{\text{inv}}(r) j_l(k). \tag{S12b}$$

As shown in Fig. S4, the function  $F_l(k)$  has a single maximum as a function of  $k$ .  $G_l(k)$  oscillates between positive and negative values when increasing  $k$ , while the amplitude decreases. When calculating the projection coefficient, it turns out that the maximal value of  $\lambda_l$  is achieved when the peak regions of  $F_l(k)$  and  $G_l(k)$  overlap.

In the limit  $k_F \bar{R} \ll 1$  ( $k_F \ll \bar{k}$ ), one can make a Taylor's expansion of  $\lambda_l$  in terms of  $k_F \bar{R}$ . The leading order of the expansion gives  $\lambda_l \sim V_0/E_F (k_F \bar{R})^{\beta_l}$  with  $\beta_l = l + 3$ . Recalling that  $V_0 = \hbar \Omega^4 / 8\delta^3$ , and  $\bar{R} \propto n^{11/6} |\delta|^{-1/6}$ , the dependence of the projection on other parameters can be obtained,  $\lambda_l \propto [n^{11\beta_l/6}, \Omega^4, |\delta|^{-3-\beta_l/6}, k_F^{\beta_l-2}]$ . In the main text, the dependence on Rydberg state ( $n$  and  $\bar{R}$ ) and Fermi momentum (atomic density) is shown in Fig. 3(b)-(c). In Fig. S5, the dependence of  $\lambda_2$  on laser parameter  $\Omega$  and  $\delta$  is given, which follows the scaling well in the perturbative regime.

- 
- [S1] N. Šibalić, J. Pritchard, C. Adams, and K. Weatherill, ARC: An open-source library for calculating properties of alkali Rydberg atoms, *Comput. Phys. Commun.* **220**, 319 (2017).
- [S2] E. Robertson, N. Šibalić, R. Potvliege, and M. Jones, ARC 3.0: An expanded Python toolbox for atomic physics calculations, *Comput. Phys. Commun.* **261**, 107814 (2021).
- [S3] E. Guardado-Sanchez, B. M. Spar, P. Schauss, R. Belyansky, J. T. Young, P. Bienias, A. V. Gorshkov, T. Iadecola, and W. S. Bakr, Quench dynamics of a fermi gas with strong nonlocal interactions, *Phys. Rev. X* **11**, 021036 (2021).
- [S4] Z. Lan, J. Minář, E. Levi, W. Li, and I. Lesanovsky, Emergent devil's staircase without particle-hole symmetry in Rydberg quantum gases with competing attractive and repulsive interactions, *Phys. Rev. Lett.* **115**, 203001 (2015).
- [S5] Z. Lan, I. Lesanovsky, and W. Li, Devil's staircases without particle-hole symmetry, *Phys. Rev. B* **97**, 075117 (2018).
- [S6] A. A. Kamenski, N. L. Manakov, S. N. Mokhnenko, and V. D. Ovsiannikov, Energy of van der Waals and dipole-dipole interactions between atoms in Rydberg states, *Phys. Rev. A* **96**, 032716 (2017).
- [S7] N. D. Woods, M. C. Payne, and P. J. Hasnip, Computing the self-consistent field in Kohn-Sham density functional theory, *J. Phys. Condens. Matter* **31**, 453001 (2019).
- [S8] A. S. Alexandrov, *Theory of superconductivity: from weak to strong coupling* (CRC Press, Boca Raton, 2003), pp. 38–39.